

See discussions, stats, and author profiles for this publication at: <https://www.researchgate.net/publication/224823106>

Molecular Thin Films on Solid Surfaces: Mechanisms of Melting

ARTICLE *in* LANGMUIR · APRIL 2012

Impact Factor: 4.46 · DOI: 10.1021/la300826p · Source: PubMed

CITATIONS

4

READS

11

4 AUTHORS, INCLUDING:



Jian Zhou

South China University of Technology

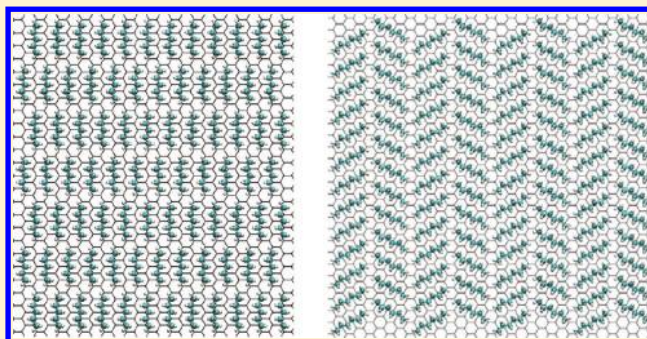
84 PUBLICATIONS 1,593 CITATIONS

SEE PROFILE

Molecular Thin Films on Solid Surfaces: Mechanisms of Melting

Haijun Feng,^{†,§} Kelly E. Becker,[†] Jian Zhou,[§] and Kristen A. Fichthorn^{*,†,‡}[†]Department of Chemical Engineering and [‡]Department of Physics, The Pennsylvania State University, University Park, Pennsylvania 16802, United States[§]School of Chemistry and Chemical Engineering, South China University of Technology, Guangzhou 510640, China

ABSTRACT: We use molecular dynamics simulations to study the melting of pentane and hexane monolayers adsorbed on the basal plane of graphite. For both of these systems, the temperature-dependent structures and the melting temperatures agree well with experiment. A detailed analysis reveals that a mechanism involving the promotion of molecules to the second layer underlies melting in these systems. In the second-layer promotion mechanism, a small fraction of molecules transition into the second layer around the melting temperature, leaving vacant space in the first layer to facilitate disordering. The second-layer promotion mechanism arises because of the weaker molecule–surface interaction in our study than that in previous studies. The weaker molecule–surface interaction is consistent with experimental temperature-programmed desorption studies.



■ INTRODUCTION

Organic thin films have been heavily studied for applications such as thin-film transistors, solar cells, and light-emitting diodes.^{1–4} Although the structures of these films are of crucial importance in determining their performance, predicting and controlling organic thin-film structures is still a challenge. From a theoretical perspective, difficulties associated with handling large molecules and the significant role played by van der Waals interactions make first-principles studies challenging for many organic thin-film systems. Although some progress has been made in understanding organic thin-film structures using molecular dynamics (MD) simulations based on force fields,^{5–18} achieving sufficiently large system sizes and adequate simulation times can be challenging. Additionally, the reliability of the force fields for these simulations, especially those for the interaction of the molecules with the solid surface, can limit their capabilities.

n-Alkane thin films are prototypical organic thin-film systems, and a great deal of theoretical^{11–18} and experimental^{19–25} effort has been directed toward understanding the low-temperature, solidlike structures and phase transitions in these systems. Theoretical efforts to understand the temperature-dependent structures measured in experimental scattering studies of these systems have shown that factors such as molecular flexibility, size, and small changes in coverage can play a significant role.^{11–18} Despite these efforts, the understanding of these systems is still not quantitative. In this work, we demonstrate that a quantitative description of the molecule–surface interaction, missing from previous studies of alkane thin films, is essential to capturing the temperature-dependent structures of these films.

We study *n*-pentane and *n*-hexane thin films on the basal plane of graphite at monolayer (ML) coverage for temperatures ranging from 0 K to melting. For the adsorption of *n*-pentane on graphite, our previous work²⁶ indicated that the alkane–surface interaction is significantly weaker than that typically assumed in MD studies of alkane thin films. By adopting a proper alkane–surface interaction, our results agree with experimental scattering studies of the temperature-dependent structures and melting of these films. However, we find that the mechanism of melting, which involves the promotion of a small fraction of molecules to the second layer of the film, is qualitatively different than the footprint reduction mechanism^{16,21} typically invoked to explain melting in these systems. Our study emphasizes the importance of considering multiple experimental inputs in parametrizing force fields, particularly those for the molecule–surface interaction, for organic thin films.

■ SIMULATION DETAILS

We consider the melting of a monolayer (ML) of either *n*-pentane (C₅H₁₂) or *n*-hexane (C₆H₁₄) adsorbed on the basal plane of graphite C(0001). In our model,^{26–28} carbon and hydrogen atoms in the alkanes are treated explicitly, and the total energy U_{total} is given by

$$U_{\text{total}} = \sum_i^N U_{\text{intra},i} + U_{\text{inter},i} + U_{\text{surf},i} \quad (1)$$

Received: February 26, 2012

Revised: April 20, 2012

Published: April 23, 2012



where $U_{\text{intra},i}$, $U_{\text{inter},i}$, and $U_{\text{surf},i}$ are the intramolecular, intermolecular, and molecule–surface interactions for molecule i , respectively, and the sum runs over all N molecules. Intermolecular and intramolecular interactions are given by the OPLS-AA force field.²⁹ We neglect Coulomb interactions because these are small for nonpolar alkane molecules. Because of their high stretching frequencies, we constrain C–C and C–H bond lengths to their equilibrium values. Similarly, we constrain H–C–H bond angles to their equilibrium values. In the MD simulations, we impose these constraints using the RATTLE algorithm.³⁰ All other internal motions, including C–C and H–C–C bends and all torsions, are modeled explicitly. Thus, the intramolecular interactions for molecule i are given by

$$U_{\text{intra},i} = U_{\theta,i} + U_{\varphi,i} + U_{\text{LJ},i} \quad (2)$$

Here, $U_{\theta,i}$ is the total bond-angle bending potential for molecule i and is given by a sum over all of its unconstrained bond angles as

$$U_{\theta,i} = \sum_j K_{\theta_j} (\theta_j - \theta_{\text{eq},j})^2 \quad (3)$$

where θ_j is the instantaneous bond angle, $\theta_{\text{eq},j}$ is the equilibrium bond angle, and K_{θ_j} is the force constant for bond angle j . The torsion potential for molecule i is given by a sum over all its torsion angles as

$$U_{\varphi,i} = \frac{1}{2} \sum_j V_1^j [1 + \cos(\varphi_j)] + V_2^j [1 - \cos(2\varphi_j)] + V_3^j [1 + \cos(3\varphi_j)] \quad (4)$$

where V_1^j , V_2^j , V_3^j are the Fourier coefficients and φ_j is the dihedral angle for torsion j .

In addition to bond-angle bending and torsion, nonbonded intramolecular interactions are important for atoms that are sufficiently far apart in the molecule. Nonbonded intramolecular interactions are given by a sum of Lennard-Jones (LJ) 12–6 pair interactions between all atoms j and k that comprise molecule i :

$$U_{\text{LJ},i} = \sum_j \sum_{k>j} 4\epsilon_{jk} \left[\left(\frac{\sigma_{jk}}{r_{jk}} \right)^{12} - \left(\frac{\sigma_{jk}}{r_{jk}} \right)^6 \right] f_{jk} \quad (5)$$

ϵ_{jk} and σ_{jk} are energy and length parameters, respectively. The factor f_{jk} is added to turn off nonbonded interactions when two atoms are sufficiently close in the molecule that their interaction is governed by bond-angle bending or torsion. For 1–3 pairs (defined as third neighbors counting bonds along a connected path in the molecule) or less, $f_{jk} = 0$; for 1–5 pairs (fifth neighbors in the molecule) and beyond, $f_{jk} = 1$ and interactions between atoms in various segments in the molecule are the same as those between atoms in different molecules. Atoms pairs that are fourth neighbors in the molecule (1–4 pairs) have $f_{jk} = 0.5$ by convention. Cross parameters for interactions between different atomic species i and j are calculated using Lorentz–Berthelot combining rules,

$$\epsilon_{ij} = \sqrt{\epsilon_{ii}\epsilon_{jj}} \quad (6)$$

and

$$\sigma_{ij} = \frac{\sigma_{ii} + \sigma_{jj}}{2} \quad (7)$$

The intermolecular interactions for molecule i are also given by a sum of LJ 12–6 pair interactions between all atoms j in molecule i and all atoms k in every other molecule. These can also be described by eq 5 with $f_{jk} = 1$ for all pairs. The parameters and combining rules for intermolecular interactions are the same as those for nonbonded intramolecular interactions. A cutoff of 11 Å is used for intermolecular interactions.

Interactions between the alkane molecules and the graphite surface are dominated by van der Waals forces and are modeled using a modified Steele potential.^{31,32} The molecule–surface interaction for molecule i is given by

$$U_{\text{surf},i} = \sum_j V_0(z_j) + sV_1(z_j)f_1(x_j, y_j) \quad (8)$$

where

$$V_0(z_j) = \frac{4\pi\epsilon_j\sigma_j^6}{a_s} \sum_{p=0}^{\infty} \left(\frac{2\sigma_j^6}{5(z_j + p\Delta z)^{10}} - \frac{1}{(z_j + p\Delta z)^4} \right) \quad (9)$$

$$V_1(z_j) = \frac{2\pi\epsilon_j\sigma_j^6}{a_s} \left[\frac{\sigma_j^6}{30} \left(\frac{g_1}{2z_j} \right)^5 K_5(g_1 z_j) - 2 \left(\frac{g_1}{2z_j} \right)^2 K_2(g_1 z_j) \right] \quad (10)$$

and

$$f_1(x_j, y_j) = -2 \left[\cos \left(\frac{4\pi x_j}{\sqrt{3}} \right) + \cos \left(\frac{2\pi x_j}{\sqrt{3}} - 2\pi y_j \right) + \cos \left(\frac{2\pi x_j}{\sqrt{3}} + 2\pi y_j \right) \right] \quad (11)$$

Here, the sum runs over all atoms j in molecule i , ϵ and σ are the energy and length parameters, respectively, for the alkane–surface interactions, G is graphite, a_s is the area of the graphite surface unit cell, Δz is the distance between graphite layers in the surface, K_i is a Bessel function of order i , and g_1 is the magnitude of the first reciprocal lattice vector. The values of a_s , Δz , and g_1 are taken from Steele's paper.³¹ The expression for U_{surf} is terminated at V_1 , meaning that lateral corrugation in the potential is due to the first layer of carbon atoms only. We choose $s = 1.5$ to provide sufficient corrugation.^{32,33} Table 1 lists all of the parameters used in this article.

All simulations in this study are run within the canonical ($N\rho T$) ensemble, where the number of molecules N , density ρ , and temperature T are constant. We use the velocity Verlet algorithm³⁴ with a time step of 1 fs to integrate the equations of motion. Periodic boundary conditions are used in the two orthogonal directions parallel to the surface, and temperature control is implemented using the Berendsen thermostat.³⁵

RESULTS AND DISCUSSION

Low-Temperature Structures of the Ordered Layers.

We first determined the ground-state structures for all-*trans* *n*-pentane and *n*-hexane MLs predicted by our model and compared them with those found in low-temperature neutron diffraction experiments.^{20,23–25} In determining these structures, we followed Hansen's procedure¹⁶ to establish that the periodic

Table 1. Parameters Used in Evaluating the Potential Energy Using Equations 3–10, Where C Is Carbon, H Is Hydrogen, and G Is Graphite

parameter	value
K_θ (kJ/mol)	156.9 (C–C–H) 244.1 (C–C–C)
θ_{eq} (deg)	110.7 (C–C–H) 112.7 (C–C–C)
V_1 (kJ/mol)	0.0 (H–C–C–H) 0.0 (H–C–C–C)
V_2 (kJ/mol)	7.28 (C–C–C–C) 0.0 (H–C–C–H) 0.0 (H–C–C–C)
V_3 (kJ/mol)	–0.657 (C–C–C–C) 1.331 (H–C–C–H) 1.531 (H–C–C–C) 1.167 (C–C–C–C)
ϵ (kJ/mol)	0.126 (H–H) 0.276 (C–C) 0.173 (C–G) 0.127 (H–G)
σ (Å)	2.50 (H–H) 3.50 (C–C) 3.40 (C–G) 2.95 (H–G)
a_s (Å ²)	5.24
Δz (Å)	3.39
g_1 (Å ^{–1})	$4\pi/3^{1/2}a_1$
a_1 (Å)	2.46
s	1.5

simulation boxes can hold integer numbers of both alkane unit cells and graphite unit cells. For a simulation box with dimensions of x_{box} and y_{box} we have

$$x_{\text{box}} = an_a = \frac{\sqrt{3}}{2}a_1n_x \quad (12)$$

and

$$y_{\text{box}} = bn_b = a_2n_y \quad (13)$$

where a and b are the dimensions of the alkane ML unit cells, as indicated in Figure 1, n_a and n_b are the corresponding (integer) numbers of alkane unit cells, a_1 and a_2 are the dimensions of the graphite unit cell (in the setup of Figure 1, $a_1 = a_2 = 2.46$ Å), and n_x and n_y are the (integer) numbers of graphite unit cells along the x and y directions, respectively. For pentane, with $n_a = 12$ and $n_b = 5$ (i.e., 120 molecules), we have

$$x_{\text{box}} = a \times 12 = 2.13n_x \quad (14)$$

and

$$y_{\text{box}} = b \times 5 = 2.46n_y \quad (15)$$

Following previous work,^{16,25} we initially tried $a = 4.67$ Å and $b = 17.01$ Å, which leads to $n_x = 26.31$ and $n_y = 34.57$. Because n_x and n_y must be integers, we set $n_x = 26$ and $n_y = 35$, which leads to $a = 4.62$ Å and $b = 17.22$ Å. Using these values in the energy minimization of an all-*trans* pentane ML, we found a virtually uniform ML with one gap in the x direction. Excluding the gap, the distance between two nearest-neighbor pentane molecules in the x direction is 4.31 Å. Thus, we adopted $a = 4.31$ Å and $b = 17.01$ Å to recalculate $n_x = 24.28$ and $n_y = 34.57$, which we rounded to $n_x = 24$ and $n_y = 35$. The resulting pentane unit cell after energy minimization had dimensions of $a = 4.26$ Å and $b = 17.22$ Å, which eliminates the gap. To ensure that the resulting pentane ML was not compressed, we performed two different energy minimizations in which we deleted a whole row or a whole column of the ML, and we found that a and b remained virtually constant for the rest of the molecules (i.e., the ML did not expand). We also tried $n_x = 25$ as well as $n_y = 36$ and 37, but gaps formed in the ML with these integer values and the total energies were all higher than the ML with $n_x = 24$ and $n_y = 35$. Thus, it appears that pentane unit cell dimensions of $a = 4.26$ Å and $b = 17.22$ Å are reasonable for our model.

For hexane, we used $n_a = 4$ and $n_b = 13$ (i.e., 104 molecules), and we took initial values for a and b from Newton's work.^{16,19,20} Following a similar procedure as for pentane, we found $a = 17.04$ Å and $b = 4.92$ Å for the hexane unit cell. The final ML unit cells are shown in Figure 1, where we see that pentane has a rectangular-centered (RC) arrangement and hexane has a herringbone (HB) structure. These ground-state

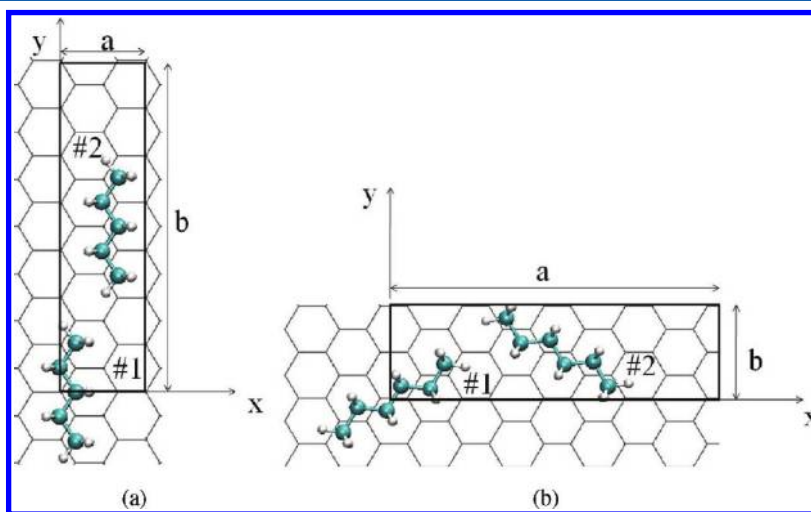


Figure 1. Schematic diagram of the ML unit cells for (a) pentane and (b) hexane. Each unit cell contains two molecules (1 and 2), and molecule 2 is in the center of the cell in panels a and b. The x and y axes are in the graphite [100] and [110] directions, respectively.

ML structures are commensurate with the graphite surface in both the x and y directions. Neutron and X-ray diffraction experiments have shown that both pentane²³ and hexane^{19,20,24} MLs are uniaxially commensurate at low coverages and fully commensurate at high coverages.

To characterize the ordered unit-cell structures further, we defined three angles specifying the molecular orientation, as shown in Figure 2, following the commonly used defini-

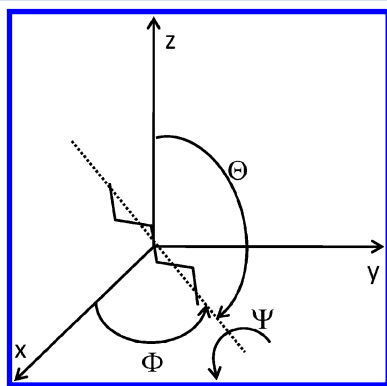


Figure 2. Definition of the three angles specifying the molecular orientation in a coordinate system fixed to the graphite substrate. The z axis is perpendicular to the graphite basal plane, and the directions of the x and y axes are defined in Figure 1. The long axis of the molecule is indicated by the dashed line. The orientation of the long axis is specified by the polar angle Θ and azimuthal angle Φ . The rolling angle Ψ describes rotation about the long axis.

tion.^{16,19,20,25} The polar angle Θ is the angle between the long axis of the molecule and the z direction perpendicular to the surface, and the in-plane azimuthal angle Φ gives the direction of the molecular long axis in the xy plane. The long axis is defined to be the principal axis of the molecule with the smallest moment of inertia. When the molecule is in the trans conformation, the principal axis with the largest moment of inertia is perpendicular to the plane of the carbon backbone. The rolling angle Ψ is the angle between this axis and the surface plane so that $\Psi = 90^\circ$ when the backbone plane is parallel to the surface for an all-trans alkane. Our calculated structural parameters for the unit cells of both molecules are compared with values obtained from neutron diffraction experiments^{20,23–25} in Tables 2 and 3. Here, we see that our calculated lattice parameters are in close agreement with those from experiments. Using a united-atom model, Hansen and Taub^{16,21} also tested the structural parameters of the hexane

Table 3. Comparison of Experimental Lattice Values to Those Calculated in This Study for a Hexane ML at Zero Temperature^a

parameter	1		2		lattice		
	calc	expt ²⁰	calc	expt ²⁰	calc	expt ²⁰	expt ²⁴
$x/\text{\AA}$	0.00	0.00	8.52	8.52			
$y/\text{\AA}$	0.00	0.00	2.46	2.46			
Ψ/deg	−89.0	−90.0	89.0	90.0			
Θ/deg	0.1	0.0	0.1	0.0			
Φ/deg	−62.7	−67.0	62.7	67.0			
$a/\text{\AA}$					17.04	17.04	16.9
$b/\text{\AA}$					4.92	4.92	4.9

^a1 and 2 represent the two molecules in the unit cell (cf. Figure 1b). x and y denote center-of-mass coordinates. The lattice constants (a , b) and angles (Ψ , Θ , Φ) are defined in Figures 1 and 2, respectively.

unit cell and found a discrepancy of $\sim 9\%$. The relatively better agreement with experiment that we find here may stem from our use of an all-atom model for hexane.

Melting. To study the melting of a pentane ML, we performed MD simulations at temperatures ranging from 0 to 250 K. In these simulations, we began with our zero-temperature ML structures and raised the temperature to 20 K. At this temperature, we performed an equilibration run for 500 ps and a production run for 500 ps to obtain statistics of the ML. Subsequently, we raised the temperature by 20 K and repeated the cycle of equilibration and production. We continued this cycle of heating, taking the equilibrated structure from a lower temperature as the initial structure for the higher temperature, in increments of 20, 10, or 5 K, until we reached a temperature of 250 K. Although the potential energy reached a constant value by the end of each equilibration run and maintained that value throughout the subsequent production run, it is possible that longer equilibration times were necessary because of very slow transients for some of the runs at the lowest temperatures.

We calculated three different quantities to characterize the melting of the layers: the average potential energy, the structural (OP_2), nematic (OP_n), and (in the case of hexane) herringbone (HB) (OP_h) order parameters, and the in-plane radial distribution function of the molecular center of mass $g(r)$. The structural order parameter is defined as

$$\text{OP}_2 = \left\langle \left| \frac{1}{N} \sum_{i=1}^N \cos(2\Phi_i) \right| \right\rangle \quad (16)$$

Table 2. Comparison of Experimental Lattice Values to Those Calculated in This Study for the Pentane ML at Zero Temperature^a

parameter	1		2		lattice		
	calc	expt ²⁵	calc	expt ²⁵	calc	expt ²⁵	expt ²³
$x/\text{\AA}$	0.00	0.00	2.13	2.34			
$y/\text{\AA}$	0.00	0.00	8.61	8.51			
Ψ/deg	89.9	90.0	89.9	90.0			
Θ/deg	0.0	0.0	0.0	0.0			
Φ/deg	0.0	0.0 \pm 5.0	0.0	0.0 \pm 5.0			
$a/\text{\AA}$					4.26	4.67 \pm 0.02	4.26
$b/\text{\AA}$					17.22	17.01 \pm 0.02	17.1

^a1 and 2 represent the two molecules in the unit cell (cf. Figure 1a). x and y denote center-of-mass coordinates. The lattice constants (a , b) and angles (Ψ , Θ , Φ) are defined in Figures 1 and 2, respectively.

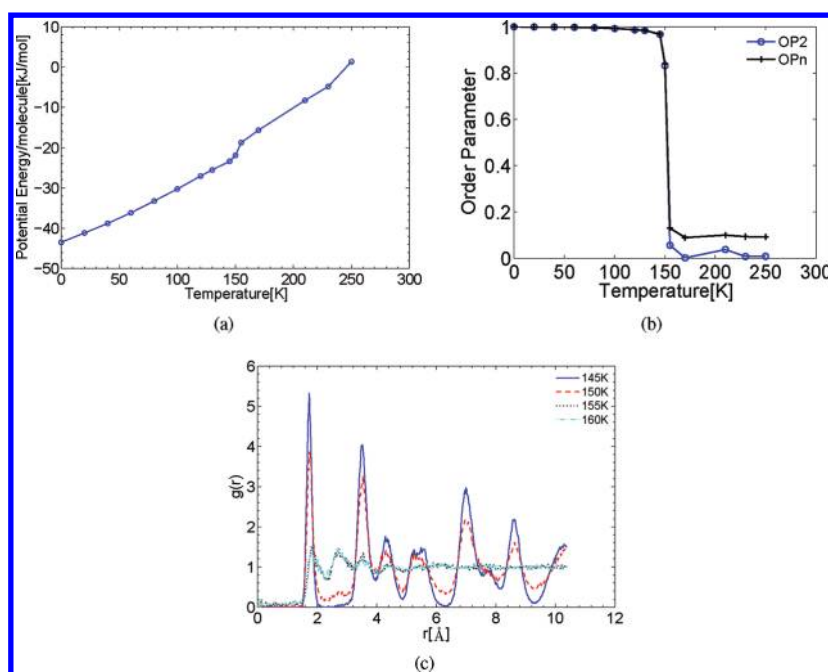


Figure 3. Evolution of (a) the potential energy, (b) OP_2 and OP_n , and (c) $g(r)$ for the pentane ML as a function of temperature.

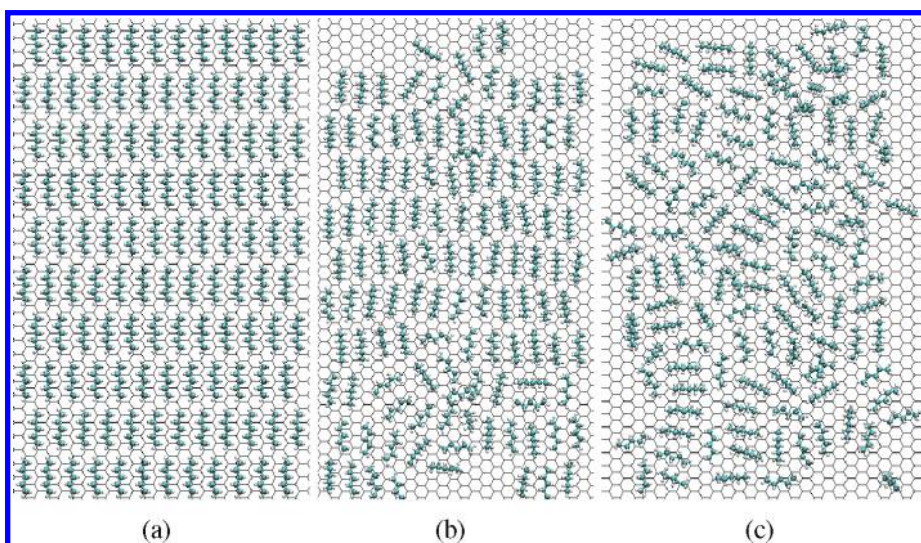


Figure 4. Snapshots of pentane MLs at (a) 0, (b) 150, and (c) 155 K. Carbons are green, and hydrogens are white.

where N is the number of molecules, Φ_i is the azimuthal angle that the long axis of molecule i makes with the x axis of the graphite cell (Figure 2), and $\langle \dots \rangle$ denotes an ensemble average. This order parameter indicates the existence of 2-fold symmetry in the solid phase. For an ordered phase, OP_2 is nonzero and assumes values close to zero when the system loses order. The nematic order parameter is defined as

$$OP_n = \left\langle \left| \frac{1}{N} \sum_{i=1}^N \cos(2(\Phi_i - \Phi_{\text{dir}})) \right| \right\rangle \quad (17)$$

where Φ_i is defined above. The director Φ_{dir} is defined as

$$\Phi_{\text{dir}} = \frac{1}{2} \tan^{-1} \left[\frac{\sum_{i=1}^N \sin(2\Phi_i)}{\sum_{i=1}^N \cos(2\Phi_i)} \right] \quad (18)$$

where the four-quadrant version of \tan^{-1} is used. The nematic order parameter quantifies the tendency of the molecular axes to be aligned in one direction and takes on nonzero values when significant alignment occurs. The HB order parameter is given by

$$OP_h = \left\langle \left| \frac{1}{N} \sum_{i=1}^N (-1)^j \sin(2\Phi_i) \right| \right\rangle \quad (19)$$

where Φ_i is defined above. The integer j is set to account for different sublattices of the HB pattern. The HB order parameter assumes high values when the system exhibits HB ordering and zero values when this type of ordering does not occur. The in-plane radial distribution function is defined as

$$g(r) = \left\langle \frac{N(r, r + \Delta r)}{2\pi r \Delta r \rho} \right\rangle \quad (20)$$

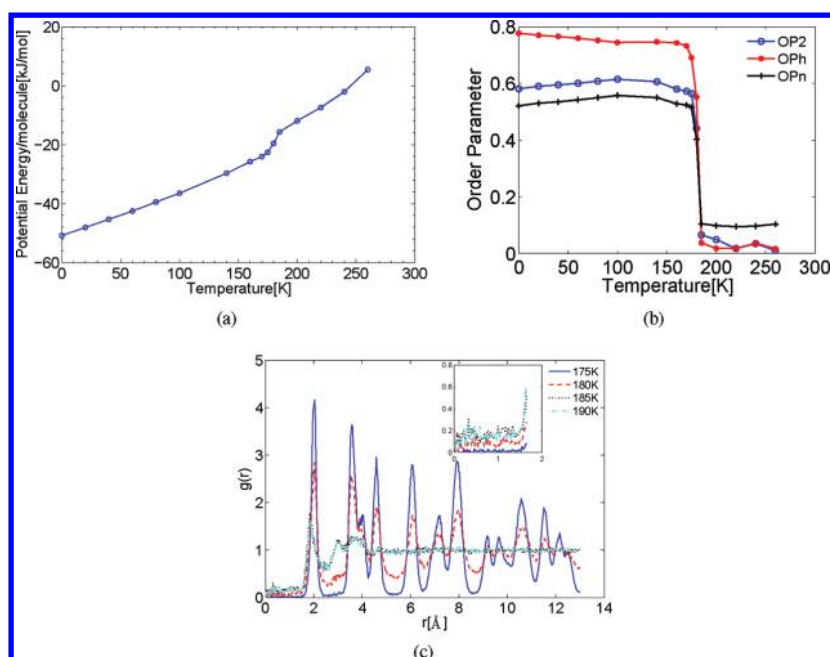


Figure 5. Evolution of (a) the potential energy, (b) OP_2 , OP_n , and OP_h , and (c) $g(r)$ for the hexane ML as a function of temperature. The inset in c shows a blow-up of the region between 0 and 2 Å.

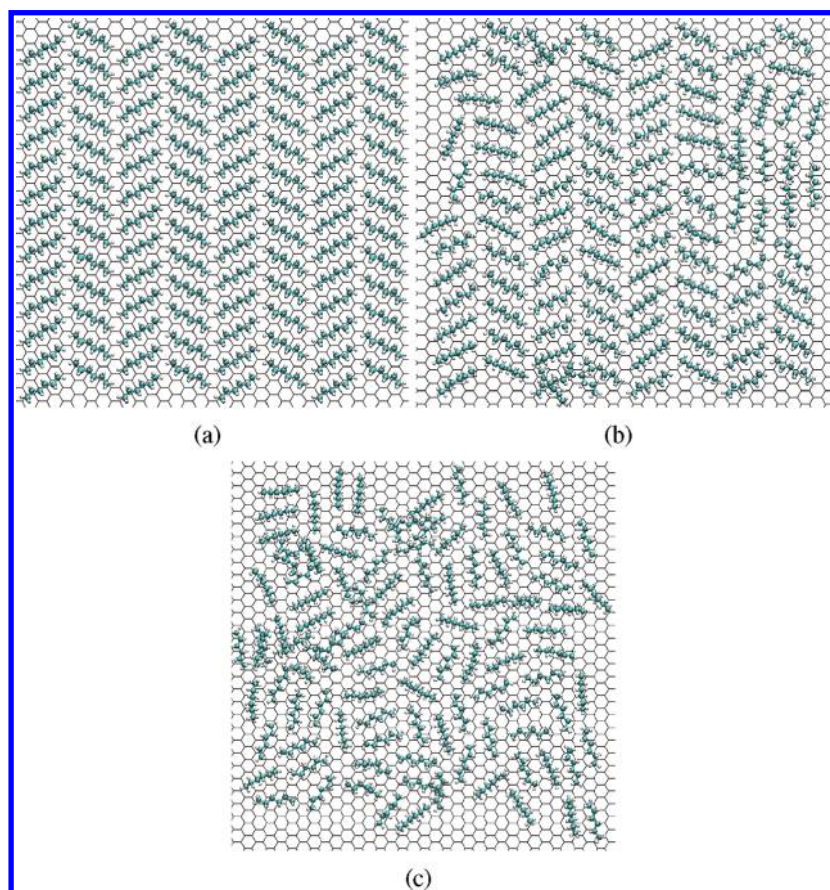


Figure 6. Snapshots of hexane MLs at (a) 0, (b) 180, and (c) 185 K. Carbons are green, and hydrogens are white.

where $N(r, r + \Delta r)$ is the number of molecules whose center-of-mass coordinates in the surface plane are between r and $r + \Delta r$ from those of a fixed molecule and ρ is the 2D center-of-mass density. Errors in calculated quantities Δx were estimated using

$$\Delta x = \left[\frac{\sum_{i=1}^{N_0} (x_i - \hat{x})^2}{N_0(N_0 - 1)} \right]^{1/2} \quad (21)$$

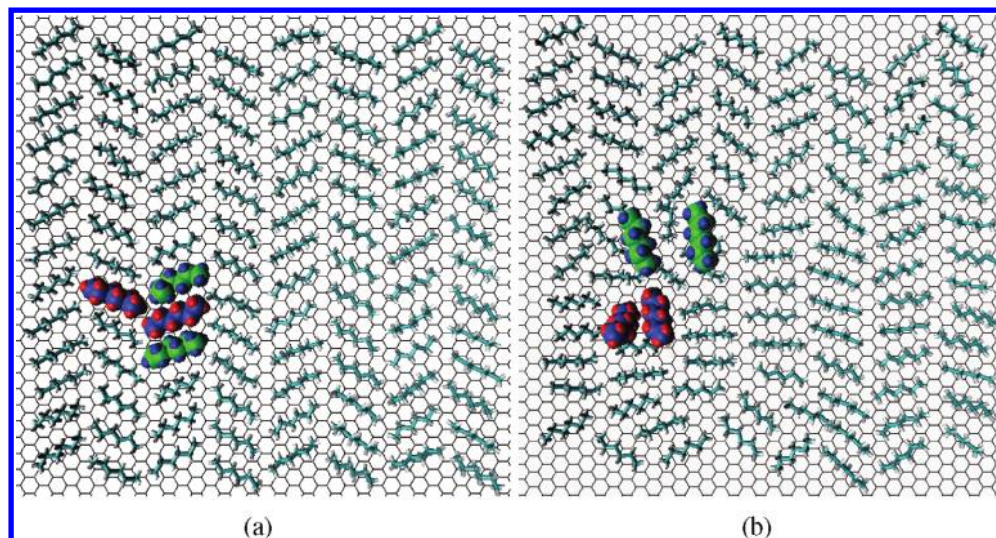


Figure 7. MD snapshots illustrating the second-layer promotion mechanism of melting in a hexane ML at 180 K. In the initial configuration (a), all of the molecules are arranged in a well-ordered HB structure. (b) Two of the molecules (shown with larger green carbons and blue hydrogens) hop above the first layer, leaving space for two neighboring molecules (shown with larger blue carbons and red hydrogens) to disorder in the resulting vacancy.

where N_o is the number of observations, \hat{x} is the mean value of x , and x_i is the value of x at step i . We calculated averages and the error in all quantities at a time interval of 5 ps. In all cases, we find that the error bars are smaller than our symbol sizes.

Pentane. In Figure 3, we characterize the melting of the pentane ML. Figure 3a shows the potential energy as a function of temperature. A jump in the energy between 150 and 155 K indicates that a phase transition occurs in this temperature range. Figure 3b shows OP_2 and OP_n as a function of temperature. Both order parameters exhibit values near unity below 150 K, indicating the prevalence of the low-temperature RC structure. There is a profound loss of order in the system between 150 and 155 K associated with melting in this temperature range. In Figure 3c, we show $g(r)$ for pentane ML at various temperatures. At temperatures of 150 K and below, $g(r)$ exhibits many peaks that are characteristic of a solid. When the temperature is 155 K or above, the peaks in $g(r)$ vanish beyond $r \approx 5 \text{ \AA}$ and $g(r)$ converges to unity at large r , which is characteristic of a liquid. Thus, the potential energy, order parameters, and radial distribution function all indicate a melting transition between 150 and 155 K. Typical configurations of the pentane layer at various temperatures are shown in Figure 4, which also indicates a melting transition from an ordered phase to a disordered phase between 150 and 155 K.

The melting temperature that we find for the pentane ML agrees with that found by Pint,¹³ who used an anisotropic united-atom model (AUA4) to model pentane overlayers in MD simulations of (near) ML melting. We also agree with the experimental results of Castro et al.,²² who used neutron diffraction to probe the melting of pentane layers adsorbed on graphite at the solid–liquid interface and found a melting temperature of 150 K. Our simulations indicate an abrupt melting transition (Figure 3), consistent with experiment.²² We note that both simulations¹³ and experiments^{22,25} indicate that the melting behavior of a pentane ML is sensitive to surface coverage: the melting temperature is lower for lower coverages. Thus, our results do not match those of Kruchten et al.,²⁵

whose experiments probed a somewhat lower coverage and found a lower melting temperature than ours.

Hexane. The hexane ML simulations were performed at temperatures between 0 and 260 K, in an analogous way to those for pentane. In Figure 5, we show the potential energy, order parameters, and in-plane radial distribution function as a function of temperature. We see discontinuous jumps in the potential energy and the order parameters between 180 and 185 K in Figure 5a,b, indicative of a melting transition. In addition, $g(r)$ exhibits solidlike peaks at 180 K, which have vanished at in-plane separations greater than $\sim 4 \text{ \AA}$ by 185 K, also pointing to a transition from a solidlike to a liquidlike structure between 180 and 185 K. Typical configurations of the hexane layer at various temperatures are shown in Figure 6, which also indicates the transition from an ordered phase to a disordered phase as the temperature increases from 180 to 185 K. Comparing this result to the experimental value of 175 K from neutron diffraction,^{19–21} we find a discrepancy of $\sim 4.3\%$.

In a recent study, Wexler et al.¹¹ also probed the melting of a hexane ML in MD simulations based on the CHARMM22 all-atom force field. Although our model is different from theirs, as we will elaborate on below, our results are similar to theirs in several respects. First, we find that the hexane ML has a direct melting transition from an HB structure to a liquid, as they found.¹¹ There is no evidence of the nematic mesophase observed in previous MD studies of (near) ML hexane melting.^{14–17} We also confirm the general melting pathway that they found, in which RC domains form and grow in size at temperatures approaching the melting temperature. Figure 5b indicates that both OP_2 and OP_n increase slightly as the temperature increases toward melting, consistent with the formation of small nematic domains. Subsequent to melting, Wexler and colleagues observed that the RC domains decrease in size with increasing temperature.¹¹ Instead of observing this decrease, we observe that OP_n increases to a peak value and begins to decrease immediately prior to melting (Figure 5b). Subsequent to melting, OP_n reaches a constant plateau value of ~ 0.1 , indicating residual nematic order. The MD snapshot shown in Figure 6c subsequent to melting indicates the

presence of small, residual nematic domains in which neighboring molecules have their long axes aligned in the RC structure. This melting scenario is consistent with experimental scattering studies.^{19–21}

Mechanisms of Melting. To elucidate the detailed melting mechanisms in these systems, we analyzed the temperature dependence of gauche defects and the tilting angle Θ (cf. Figure 2) between the long axis of the molecule and the surface. These quantities have been proposed to contribute to the footprint-reduction mechanism of melting whereby a molecule creates vacancies in the layer by tilting away from the surface and/or forming gauche defects.²¹ Vacancies formed by footprint reduction facilitate disordering of the layer and hence promote melting. We note that evidence for footprint reduction has been observed in previous MD studies of melting in alkane layers.^{11–13,15,16,21} In our study, we observe a qualitatively different mechanism in which molecules tend to jump to the second layer, remain there for a brief time, and then re-enter the first layer in a second-layer promotion mechanism that leaves vacancies in the first layer. Figure 7 shows a sequence of MD snapshots illustrating this mechanism. Because these vacancies free up space for first-layer molecules to disorder, they also facilitate melting. We note that the role of second-layer promotion in the melting transition was first discussed by Abraham in his MD studies of the melting of Xe on graphite.³⁶ To assess the importance of second-layer promotion in facilitating melting, we also analyze the fraction of the total number of molecules in the second layer as a function of temperature. In this analysis, a molecule is considered to be in the second layer if the height of all of its atoms is above the average height of the ML.

Pentane. In Figure 8a, we plot the fraction of pentane molecules in the second layer along with the fraction containing one or more gauche defects as a function of temperature. Here, we see that the fraction of molecules with gauche defects remains constant at its low-temperature value throughout the melting window and begins to increase only subsequent to melting. This indicates that there is little connection between gauche defects and melting for pentane. The fraction of molecules in the second layer exhibits a more substantial increase from a near-zero value at and below the beginning of the melting window (150 K) to 4.4% at the end of the melting window (155 K). Figure 8b shows the fraction of pentane molecules with various tilt angles. Unlike the fraction in the second layer, the fraction of molecules with a tilt angle greater than Θ increases continuously with increasing temperature up to the beginning of the melting window, where it exhibits a discontinuous jump. The magnitude of the jump from the beginning to the end of the melting window ranges from 4.3% for $\Theta \geq 5^\circ$ to 5.1% for $\Theta \geq 20^\circ$. Thus, both tilting (which leads to footprint reduction) and second-layer promotion play a role in the melting of the pentane ML.

Hexane. The fractions of gauche defects, second-layer molecules, and molecules with tilt angles greater than Θ are shown as a function of temperature for the hexane ML in Figure 9. In Figure 9a, we see that the fractions of gauche defects and second-layer molecules both exhibit discontinuous jumps around the melting window. At 2.3%, the increase in the fraction of molecules with gauche defects is larger for hexane than it is for pentane. However, the increase is still relatively small. The jump in the fraction of second-layer hexane molecules from near zero prior to melting to 9.5% at the end of the melting window is dramatic and indicates that second-

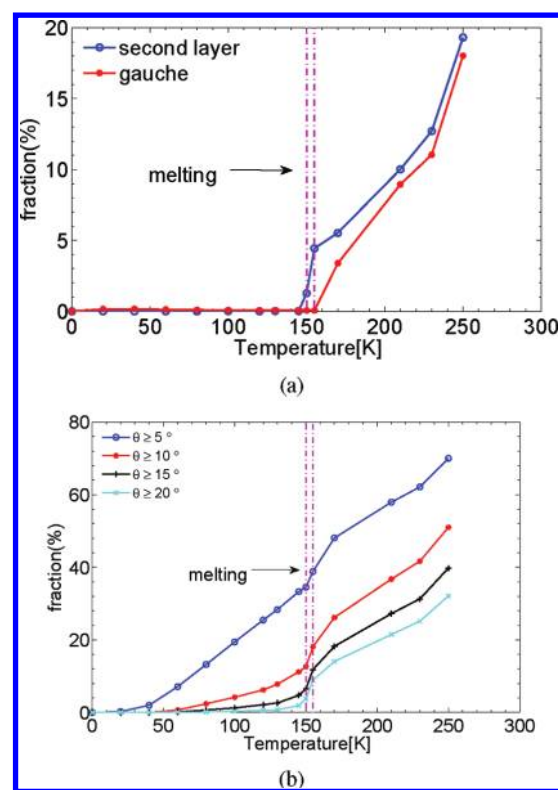


Figure 8. Indicators of the melting mechanism for the pentane ML. (a) Fraction of molecules with at least one gauche defect and fraction of molecules that reside in the second layer as a function of temperature. (b) Fraction of molecules with tilt angles greater than or equal to Θ for various values of Θ as a function of temperature. The dashed-dotted lines indicate the temperature window over which melting occurs.

layer promotion plays a significant role in the melting of the hexane ML. Evidence for second-layer molecules can also be seen in the in-plane radial distribution function for hexane in the inset of Figure 5c. Here, we see that $g(r)$ is slightly greater than zero when r is smaller than ~ 1.7 Å at 185 K and above but negligible at 180 K and below. Because the in-plane radial distribution function is calculated in the two orthogonal directions parallel to the surface, the only way for two molecules to be this close without overlapping is by residing in two different layers. Similar to pentane, the fraction of molecules with a tilt angle greater than Θ increases continuously with increasing temperature up to the beginning of the melting window, where it exhibits a discontinuous jump (Figure 9b). The magnitude of the jump from the beginning to the end of the melting window ranges from 4% for $\Theta \geq 5^\circ$ to 2% for $\Theta \geq 20^\circ$. Thus, similar to pentane, both tilting and second-layer promotion play a role in the melting of hexane ML. In the case of hexane, we find that the role of second-layer promotion is significant and this finding appears to be unique to our study.

DISCUSSION

Thus, we characterized melting in MD studies of two model systems representing pentane and hexane ML adsorbed on the basal plane of graphite. The trends that we observe here are consistent with experimental studies^{19–24} as well as with the most recent MD studies for pentane¹³ and hexane.¹¹ However, the underlying mechanisms of melting appear to be unique to

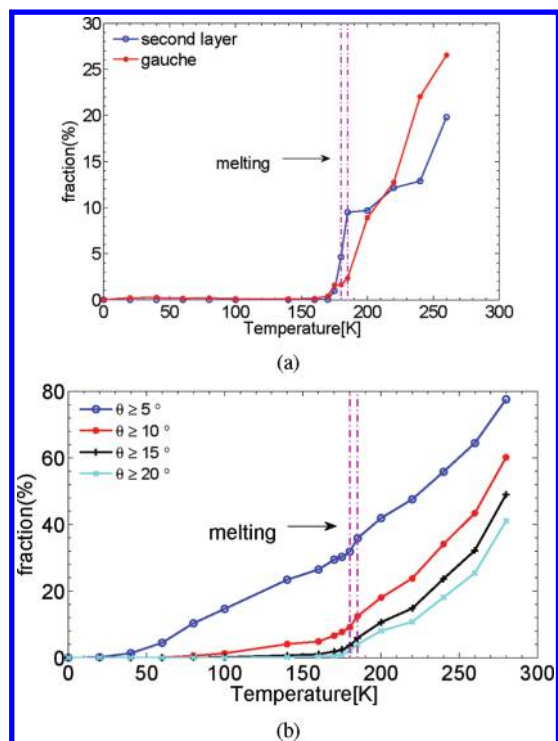


Figure 9. Indicators of the melting mechanism for the hexane ML. (a) Fraction of molecules with at least one gauche defect and fraction of molecules that reside in the second layer as a function of temperature. (b) Fraction of molecules with tilt angles greater than or equal to Θ for various values of Θ as a function of temperature. The dashed-dotted lines indicate the temperature window over which melting occurs.

our study. We observe melting trends similar to those observed by Pint,¹³ who adopted the AUA4 model for pentane chains. We also appear to confirm the trend in that study that molecular flexibility (i.e., the formation of gauche defects) does not contribute to the melting of pentane. Instead, we find that the tilting of the molecules away from the surface and the promotion of a small fraction of the molecules to the second layer are what appear to facilitate melting.

The study by Wexler and colleagues¹¹ was apparently the first in a long line of MD studies^{12,14,15,17,21} that was successful at resolving the major experimentally observed features in the melting of hexane ML on graphite. We are approximately equally successful at describing the melting transition, although the melting temperature that we find is about 5–10° higher than in the experiment. The claim in the Wexler study is that achieving zero spreading pressure in the simulation, by correct choice of the hexane unit cell, is important in securing agreement with experiment. We note that the unit cell that we determined for the hexane ML (Table 3) is in excellent agreement with experiment and has a somewhat lower area per molecule (41.92 Å²/molecule) than theirs (45.14 Å²/molecule).¹¹ We note that both simulations¹³ and experiments^{22,25} indicate that the melting behavior of a pentane ML is sensitive to surface coverage: the melting temperature is lower for lower coverages. Thus, it is possible that we could have achieved a lower melting temperature by adopting a larger unit cell for hexane. However, such a cell would not provide the minimum-energy structure for the present potential.

A second feature important in achieving the correct melting temperature is molecular flexibility. Molecular flexibility was shown to be important in influencing the melting temperature

in previous MD studies, which demonstrated that the melting transition could be pushed to higher temperatures by altering the torsion potential to inhibit the formation of gauche defects.^{13,21} Connolly et al.¹² used the CHARMM22 all-atom force field to study the melting of hexane layers and found that the appearance of the nematic mesophase prior to melting was linked to the formation of gauche defects. In their study, Wexler and colleagues altered the molecular flexibility by changing the f_{jk} factor in eq 5 (for 1–4 pairs) from the commonly used value of $f_{14} = 0.5$ (the value that we use here) to a value of $f_{14} = 0.8$. This also inhibits the formation of gauche defects because larger values of the scaling factor lead to the suppression of gauche defects until higher temperatures are reached.¹⁸ We note that changing the value of f_{14} will also alter the properties of fluid-phase hexane because the CHARMM22 potential was fit by assuming $f_{14} = 0.5$. Here, we do not observe a significant fraction of molecules with gauche defects until temperatures higher than the melting window are reached. This is due to differences in the parametrization of the CHARMM22 and OPLS-AA force fields: The CHARMM22 force field tends to underestimate torsional barriers and energies for gauche conformers of hexane compared to ab initio values,³⁷ whereas the OPLS-AA force field tends to overestimate these values.^{38,39} When torsion is inhibited, gauche defects play a smaller role in footprint reduction. Here, they play no role for pentane and only a small role for hexane.

Another significant (and apparently unique) factor contributing to the success of our model is that the alkane–surface interaction is weaker than in previous models.^{11–18} Velasco and Peters pointed out that the molecule–surface interaction could play a profound role in dictating the melting temperature in hexane ML on graphite,¹⁷ although the lowest value that they considered for ϵ_C (which governs the alkane–surface interaction) is larger than our value. In a previous study,²⁶ we used our model to simulate the temperature-programmed desorption (TPD) of pentane from the basal plane of graphite, and our simulated spectrum for a pentane ML agrees well with experiment,^{40,41} with a discrepancy in the peak temperature of $\sim 1^\circ$. TPD is the most common way to assess the binding energy of a molecule to a solid surface experimentally, so matching the TPD spectrum is a strong indication that we are accurately capturing the alkane binding strength.

One aspect to emphasize in our studies of alkane desorption^{26–28} is the important role of alkane–alkane interactions in determining the overall binding energy of an alkane molecule to a solid surface. Assuming $\epsilon_{CG} = 0.291$ kJ/mol and $\epsilon_{HG} = 0.214$ kJ/mol for the interaction of C and H atoms in the alkane with atoms in the graphite surface (close to the values used by Wexler and co-workers¹¹), we were able to match various simulated *n*-alkane binding energies for the desorption of single molecules to experimental binding energies obtained at near-monolayer coverage.²⁷ In single-molecule simulations, there are no intermolecular interactions, and a larger molecule–surface interaction was needed to mimic this attraction. However, when we simulated desorption from a pentane ML, we found that these values for the molecule–surface interaction were too high and we needed to use the present values to match experimental TPD spectra.²⁶ With a weaker molecule–surface interaction, the relative importance of the molecule–molecule interaction increases, allowing second-layer promotion to occur at temperatures around the melting window. The vacancies created by second-layer molecules allow the layer to disorder so that melting occurs.

CONCLUSIONS

We presented a model for the adsorption of pentane and hexane on the basal plane of graphite, and we used MD simulations based on this model to probe the melting of pentane and hexane MLs. For both of these molecules, we achieve good agreement with experimental studies on all measured aspects of melting. A second feature of our model is that it can reproduce experimental TPD spectra for pentane desorption from graphite.²⁶

We emphasize that two features of our model appear to be unique. First, the alkane–surface interaction is weaker in our study than in previous studies. This weaker interaction leads to the promotion of a small fraction of molecules into the second layer at temperatures in the melting window. The vacancies created by second-layer molecules allow the first layer to disorder so that melting occurs. A second unique feature of our model is that we employ the OPLS-AA force field to describe inter- and intramolecular alkane interactions. Apparently, the energies for gauche states are higher in this model than those in previous studies of alkane melting so that gauche defects play no role in the melting transition of pentane and only a small role in the melting of hexane. This leads to an abrupt HB → liquid transition, where small nematic domains appear and grow prior to melting and then persist in the midst of a disordered liquidlike phase subsequent to melting. In addition to second-layer promotion, we observe a jump in the out-of-plane tilting of the long axes of both molecules over their melting windows. By tilting away from the surface, a molecule reduces its footprint in the layer and creates free space for melting. Thus, our results indicate that a combination of footprint reduction and second-layer promotion underlies melting in these systems.

Another point that arises in this study is that the melting in these systems arises from an intricate combination of interactions, and by comparing our study with those of Pint¹³ and Wexler and colleagues,¹¹ we see that this combination is not unique. This indicates that to achieve a firm understanding of the structure and function of organic thin films, a holistic view is needed, with a focus that is broader than a single experimental measure. Here, we match the low-temperature unit cell inferred from experimental scattering studies, the melting temperature, and the molecule–surface interaction revealed in experimental TPD studies. Such an approach will ultimately be useful in designing organic thin-film structures.

AUTHOR INFORMATION

Corresponding Author

*E-mail: fichthorn@psu.edu.

Notes

The authors declare no competing financial interest.

ACKNOWLEDGMENTS

We acknowledge useful discussions with Flemming Hansen, Maria Mignogna, Yogesh Tiwary, and Yangzheng Lin. This research was supported by the National Science Foundation (grants DGE 9987589 and DMR 0514336) and the China Scholarship Council.

REFERENCES

- (1) Forrest, S. R. Ultrathin Organic Films Grown by Organic Molecular Beam Deposition and Related Techniques. *Chem. Rev.* **1997**, *97*, 1793–1896.
- (2) Dimitrakopoulos, C. D.; Malenfant, P. R. L. Organic Thin Film Transistors for Large Area Electronics. *Adv. Mater.* **2002**, *14*, 99–117.
- (3) Peumans, P.; Yakimov, A.; Forrest, S. R. Small Molecular Weight Organic Thin-Film Photodetectors and Solar Cells. *J. Appl. Phys.* **2003**, *93*, 3693–3723.
- (4) Djuric, T.; Ules, T.; Gusenleitner, S.; Kayunkid, N.; Plank, H.; Hlawacek, G.; Teichert, C.; Brinkmann, M.; Ramsey, M.; Resel, R. Substrate Selected Polymorphism of Epitaxially Aligned Tetraphenyl-Porphyrin Thin Films. *Phys. Chem. Chem. Phys.* **2012**, *14*, 262–272.
- (5) Muccioli, L.; D'Avino, G.; Zannoni, C. Simulation of Vapor-Phase Deposition and Growth of a Pentacene Thin Film on C₆O (001). *Adv. Mater.* **2011**, *23*, 4532–4536.
- (6) Beljonne, D.; Cornil, J.; Muccioli, L.; Zannoni, C.; Brédas, J. L.; Castet, F. Electronic Processes at Organic–Organic Interfaces: Insight from Modeling and Implications for Opto-electronic Devices. *Chem. Mater.* **2011**, *23*, 591–609.
- (7) Chang, J.; Sandler, S. I. Free Energy of the Solid C₆₀ Fullerene Orientational Order-Disorder Transition. *J. Chem. Phys.* **2006**, *125*, 054705.
- (8) Clancy, P. Application of Molecular Simulation Techniques to the Study of Factors Affecting the Thin-Film Morphology of Small-Molecule Organic Semiconductors. *Chem. Mater.* **2011**, *23*, 522–543.
- (9) Delle Valle, R. G.; Venuti, E.; Brillante, A.; Girlando, A. Molecular Dynamics Simulations for a Pentacene Monolayer on Amorphous Silica. *Chem. Phys. Chem.* **2009**, *10*, 1783–1788.
- (10) Mansfeld, S. C. B.; Fritz, T. Advanced Modelling of Epitaxial Ordering of Organic Layers on Crystalline Surfaces. *Mod. Phys. Lett. B* **2006**, *20*, 585–605.
- (11) Wexler, C.; Firlej, L.; Kuchta, B.; Roth, M. W. Melting of Hexane Monolayers Adsorbed on Graphite: The Role of Domains and Defect Formation. *Langmuir* **2009**, *25*, 6596–6598.
- (12) Connolly, A. J.; Roth, M. W.; Gray, P. A.; Wexler, C. Explicit Hydrogen Molecular Dynamics Simulations of Hexane Deposited onto Graphite at Various Coverages. *Langmuir* **2008**, *24*, 3228–3234.
- (13) Pint, C. L. Different Melting Behavior in Pentane and Heptane Monolayers on Graphite: Molecular Dynamics Simulations. *Phys. Rev. B* **2006**, *73*, 045415.
- (14) Pint, C. L.; Roth, M. W.; Wexler, C. Behavior of Hexane on Graphite at Near-Monolayer Densities: Molecular Dynamics Study. *Phys. Rev. B* **2006**, *73*, 085422.
- (15) Roth, M. W.; Pint, C. L.; Wexler, C. Phase Transitions in Hexane Monolayers Physisorbed onto Graphite. *Phys. Rev. B* **2005**, *71*, 155427.
- (16) Hansen, F. Y.; Newton, J. C.; Taub, H. Molecular-Dynamics Studies of the Melting of Butane and Hexane Monolayers Adsorbed on the Basal-Plane Surface of Graphite. *J. Chem. Phys.* **1993**, *98*, 4128–4141.
- (17) Velasco, E.; Peters, G. H. Effect of Substrate Potential Strength on the Melting Temperature of a Hexane Monolayer Adsorbed on Graphite. *J. Chem. Phys.* **1995**, *102*, 1098–1099.
- (18) Firlej, L.; Kuchta, B.; Roth, M. W.; Wexler, C. Molecular Simulations of Intermediate and Long Alkanes Adsorbed on Graphite: Tuning of Non-Bond Interactions. *J. Mol. Model.* **2011**, *17*, 811–816.
- (19) Krim, J.; Suzanne, J.; Shechter, H.; Wang, R.; Taub, H. A Leed and Neutron-Diffraction Study of Hexane Adsorbed on Graphite in the Monolayer Range - Uniaxial Commensurate Incommensurate Transition. *Surf. Sci.* **1985**, *162*, 446–451.
- (20) Newton, J. C. Ph.D. Dissertation. University of Missouri—Columbia, 1989.
- (21) Hansen, F. Y.; Taub, H. Melting Mechanism in Monolayers of Flexible Rod-Shaped Molecules. *Phys. Rev. Lett.* **1992**, *69*, 652–655.
- (22) Castro, M. A.; Clarke, S. M.; Inaba, A.; Arnold, T.; Thomas, R. K. Anomalous Behaviour of Pentane Adsorbed at the Graphite/Liquid Interface. *Phys. Chem. Chem. Phys.* **1999**, *1*, S203–S207.
- (23) Arnold, T.; Dong, C. C.; Thomas, R. K.; Castro, M. A.; Perdigon, A.; Clarke, S. M.; Inaba, A. The Crystalline Structures of the Odd Alkanes Pentane, Heptane, Nonane, Undecane, Tridecane and Pentadecane Monolayers Adsorbed on Graphite at Submonolayer

Coverages and from the Liquid. *Phys. Chem. Chem. Phys.* **2002**, *4*, 3430–3435.

(24) Arnold, T.; Thomas, R. K.; Castro, M. A.; Clarke, S. M.; Messe, L.; Inaba, A. The Crystalline Structures of the Even Alkanes Hexane, Octane, Decane, Dodecane and Tetradecane Monolayers Adsorbed on Graphite at Submonolayer Coverages and from the Liquid. *Phys. Chem. Chem. Phys.* **2002**, *4*, 345–351.

(25) Kruchten, F.; Knorr, K.; Volkmann, U. G.; Taub, H.; Hansen, F. Y.; Matthies, B.; Herwig, K. W. Ellipsometric and Neutron Diffraction Study of Pentane Physisorbed on Graphite. *Langmuir* **2005**, *21*, 7507–7512.

(26) Becker, K. E.; Mignogna, M. H.; Fichthorn, K. A. Accelerated Molecular Dynamics of Temperature-Programmed Desorption. *Phys. Rev. Lett.* **2009**, *102*, 046101.

(27) Becker, K. E.; Fichthorn, K. A. Accelerated Molecular Dynamics Simulation of the Thermal Desorption of n-Alkanes from the Basal Plane of Graphite. *J. Chem. Phys.* **2006**, *125*, 184706.

(28) Fichthorn, K. A.; Becker, K. E.; Miron, R. A. Molecular Simulation of Temperature-Programmed Desorption. *Catal. Today* **2007**, *123*, 71–76.

(29) Jorgensen, W. L.; Maxwell, D. S.; Tirado-Rives, J. Development and Testing of the OPLS All-Atom Force Field on Conformational Energetics and Properties of Organic Liquids. *J. Am. Chem. Soc.* **1996**, *118*, 11225–11236.

(30) Andersen, H. C. Rattle - A Velocity Version of the Shake Algorithm for Molecular-Dynamics Calculations. *J. Comput. Phys.* **1983**, *52*, 24–34.

(31) Steele, W. A. Physical Interaction of Gases with Crystalline Solids 0.1. Gas-Solid Energies and Properties of Isolated Adsorbed Atoms. *Surf. Sci.* **1973**, *36*, 317–352.

(32) Kim, H. Y.; Steele, W. A. Computer-Simulation Study of the Phase-Diagram of the CH₄ Monolayer on Graphite - Corrugation Effects. *Phys. Rev. B* **1992**, *45*, 6226–6233.

(33) Vidali, G.; Cole, M. W. Lateral Variation of the Physisorption Potential for Noble-Gases on Graphite. *Phys. Rev. B* **1984**, *29*, 6736–6738.

(34) Allen, M. P.; Tildesley, D. J. *Computer Simulation of Liquids*; Clarendon Press: Oxford, U.K., 1987.

(35) Berendsen, H. J. C.; Postma, J. P. M.; Vangunsteren, W. F.; Dinola, A.; Haak, J. R. Molecular-Dynamics with Coupling to an External Bath. *J. Chem. Phys.* **1984**, *81*, 3684–3690.

(36) Abraham, F. F. Melting Transition of Near-Monolayer Xenon Films on Graphite: A Computer Simulation Study. *Phys. Rev. Lett.* **1983**, *50*, 978–981.

(37) Feller, S. E.; MacKerell, A. D., Jr. An Improved Empirical Potential Energy Function for Molecular Simulations of Phospholipids. *J. Phys. Chem. B* **2000**, *104*, 7510–7515.

(38) Price, M. L. P.; Ostrovsky, D.; Jorgensen, W. L. Gas-Phase and Liquid-State Properties of Esters, Nitriles, and Nitro Compounds with the OPLS-AA Force Field. *J. Comput. Chem.* **2001**, *22*, 1340–1352.

(39) Siu, S. W. I.; Pluhackova, K.; Böckmann, R. A. Optimization of the OPLS-AA Force Field for Long Hydrocarbons. *J. Chem. Theory Comput.* **2012**, *8*, 1459–1470.

(40) Paserba, K.; Gellman, A. Kinetics and Energetics of Oligomer Desorption from Surfaces. *Phys. Rev. Lett.* **2001**, *86*, 4338–4341.

(41) Paserba, K.; Gellman, A. Effects of Conformational Isomerism on the Desorption Kinetics of n-Alkanes From Graphite. *J. Chem. Phys.* **2001**, *115*, 6737–6751.